An Efficient Hybrid Model for 3D Complex Fractured Vuggy Reservoir Simulation

Lijun Liu, Zhaoqin Huang*, and **Jun Yao*,** China University of Petroleum (East China); **Yuan Di,** Peking University; and **Yu-Shu Wu,** Colorado School of Mines

Summary

Fractured vuggy reservoir is a typical type of carbonate reservoir. The 3D complex fracture networks and Stokes flow inside vugs make fractured vuggy reservoir simulation remain a challenging problem. Most of the proposed models in previous studies are computation consuming, which cannot meet with the demand of field application. In this paper, a novel and efficient hybrid model, consisting of a modified embedded discrete fracture model (EDFM) and a vug model, is proposed to simulate multiphase flow in 3D complex fractured vuggy reservoirs. The modified EDFM improves the fracture-discretization process by using two sets of independent grids for matrix and fracture systems, which promotes the modeling of 3D complex fractures in real geological structures. Meanwhile, the vug model simplifies the coupled porous-free flow with the assumption of multiphase instantaneous gravity differentiation. The accuracy of the modified EDFM and the vug model is demonstrated by comparing the results with those of the conventional EDFM and volume of fluid (VOF) method. After that, a series of case studies, including three conceptual fracture-vug unit models and a real field model, have been conducted to test the proposed hybrid model. The results of the three fracture-vug unit models indicate the significant effect of a local fracture-vug structure on the flow characteristics and production performance. Finally, the application with a real field model with 3D complex fracture and vug geometries further verifies the practicability of our proposed model in real fractured vuggy reservoirs.

Introduction

In the past decades, carbonate reservoirs have always been an important source of oil and gas. They are usually characterized by the well-developed fractures and vugs due to the tectonic movement and paleokarst dissolution effects (Loucks 1999; Smosna et al. 2005; Lyu et al. 2017). However, because of the complex fracture and vug geometries and flow patterns, numerical simulation of fluid flow in fractured vuggy media has always been a challenging problem. Many efforts have been made in modeling fractured vuggy reservoirs (Popov et al. 2009; Yao et al. 2010; Huang et al. 2011; Wu et al. 2011).

The commonly used models for analyzing flow in a fractured vuggy reservoir can be divided into two categories. The first category is the continuum model such as dual-porosity, dual-permeability, and multiple-porosity models. Warren and Root (1963) firstly introduced the dual-porosity model into the petroleum industry for the single-phase flow in fractured reservoirs, in which the interconnected fractures are assumed to be in sugar-cube configuration and main flow paths, while the matrix only provides storage for fluid. Later, dual-porosity was extended to dual-permeability for single-phase and multiphase flow (Chen 1989; Quandalle and Sabathier 1989; Guo et al. 2012). In addition to the dual porosity/permeability models, a number of triple porosity models have been proposed to take into consideration of vugs. In particular, Camacho-Velazquez et al. (2002) and Liu et al. (2003) presented several triple continuum models for single-phase flow in fractured vuggy system, and Kang et al. (2006) and Wu et al. (2011) further proposed a triple continuum model for multiphase flow with consideration of different local fracture and vug configurations. However, considering the assumption of regular fracture/vug configuration, these models are simplistic representations of geologically complex reservoirs, which cannot well describe the realistic fracture and vug geometries. To resolve these problems, discrete medium models have been developed, such as discrete fracture network model (DFN) (Karimi-Fard et al. 2004; Huang et al. 2014), EDFM (Lee et al. 1999; Xu et al. 2017; Zhang et al. 2017; Yan et al. 2018, 2019), and discrete fracture-vug network model (DFVN) (Yao et al. 2010). For DFN, the generation of the conformal unstructured meshes for complex fracture networks is the key step. However, the complex fracture geometries bring great difficulties to the meshing process, especially when the fractures are highly developed. Furthermore, the DFN is not well compatible with the geological model established by corner-point grids. Then the EDFM, a kind of nonconformal method which avoids the meshing process of complex fracture networks, was proposed (Lee et al. 2001; Li and Lee 2008). EDFM simplified the meshing problem by directly incorporating the fractures into the background grid, and linking the fractures and matrix with additional non-neighbor connections and transmissibility. Recently, EDFM has been implemented in various complex problems, such as nonvertical fractures (Moinfar et al. 2014) and fracture modeling in corner-point grid systems (Panfili and Cominelli 2014; Fumagalli et al. 2016; Xu and Sepehrnoori 2019; Xu et al. 2019). Xu and Sepehrnoori (2019) gives the detailed algorithms and workflow for the implementation of EDFM in corner-point grids. Furthermore, to take into consideration of vugs, DFVN was developed to handle the coexistence of porous flow in matrix and fractures and free flow in vugs. In DFVN, Darcy's law is used for the flow in porous rock and fractures, Navier–Stokes equations are used for the free flow in vugs, and the two governing equations are coupled by Beavers–Joseph–Staffman (Beavers and Joseph 1967; Saffman 1971) interface conditions. More complexity can be introduced under multiphase flow condition. Huang et al. (2016) and Xie et al. (2017) presented coupled two-phase porous-free flow model and its corresponding numerical scheme. However, the high computational complexity limits its use in real field-scale simulation. Therefore, for most of the above models, there are still some drawbacks for the application in 3D complex fractured vuggy reservoirs.

To this end, an efficient hybrid model was proposed for the characterization and simulation of 3D complex fractured vuggy reservoirs. In the hybrid model, a modified EDFM is used for handling 3D complex fracture geometry and flexible incorporation into variable grid systems, such as structured, unstructured, and corner-point grids. Moreover, a simplified vug model is developed to describe the coupled porous-free flow region near vugs. Finally, on the basis of the proposed hybrid model, simulations are carried out on a series of conceptual models and one real field model, and the results show the accuracy and practicability of the hybrid model.

* Corresponding authors.

Original SPE manuscript received for review 14 February 2019. Revised manuscript received for review 19 October 2019. Paper (SPE 199899) peer approved 21 October 2019.

Hybrid Model for Fractured Vuggy Reservoir

Mathematical Model. An isothermal black oil system in fractured vuggy reservoirs is considered in this paper. The fluid flow in porous matrix and fractures is assumed to follow Darcy's law, and the multiphase flow in vugs is simplified into instantaneous gravity differentiation, which will be discussed in the Vug Model subsection. Therefore, the mass-balance equations for multiphase flow in porous matrix and fractures can be expressed as (Aziz and Settari 1979)

$$-\nabla \cdot (\rho_o \boldsymbol{v}_o) + q_o = \frac{\partial(\phi \rho_o S_o)}{\partial t}, \quad (1)$$

$$-\nabla \cdot (\rho_{go} \boldsymbol{v}_o + \rho_g \boldsymbol{v}_g) + q_g = \frac{\partial[\phi(\rho_{go} S_o + \rho_g S_g)]}{\partial t}, \quad (2)$$

$$-\nabla \cdot (\rho_w \boldsymbol{v}_w) + q_w = \frac{\partial(\phi \rho_w S_w)}{\partial t}, \quad (3)$$

where the Darcy's velocity of phase β ($\beta = o, g, w$ for oil, gas, and water) is defined as

$$\boldsymbol{v}_\beta = -\frac{\boldsymbol{k} k_{r\beta}}{\mu_\beta} \cdot \nabla \psi_\beta; \quad (4)$$

ρ_o and ρ_{go} are the density of oil and gas component in oil phase; ρ_g and ρ_w are the density of gas and water phase at reservoir conditions; q_β is the sink/source term of phase β for unit volume of medium; ϕ is porosity; S_β is the saturation of phase β; $\boldsymbol{k}$ is the absolute permeability tensor, which can be characterized by a diagonal tensor with two principal permeabilities for 2D and three for 3D when the axes are aligned with the principal directions. For simplicity, the permeability tensor $\boldsymbol{k}$ is written as a scalar k in the following equations because only isotropic problems are involved in our study; $k_{r\beta}$ is the relative permeability of phase β; μ_β is the viscosity of phase β; ψ_β is the flow potential of phase β, defined as $\psi_\beta = p_\beta - \rho_\beta g D$; p_β is the pressure of phase β; g is the gravitational acceleration; D is the depth.

In addition to the above equations, there are constitutive equations for the system

$$S_o + S_g + S_w = 1, \quad (5)$$

$$p_w = p_o - p_{\text{cow}}, \quad (6)$$

$$p_g = p_o - p_{\text{cog}}, \quad (7)$$

where p_{cow} and p_{cog} are the oil/water and oil/gas capillary pressure.

Numerical Formulation. To numerically solve the fluid flow equation system, Eqs. 1–3 are discretized in space by integral finite difference method, and time discretization is carried out with a first-order backward finite difference scheme. The discretized governing equations are written as follows:

$$\sum_{j \in N_i} [(\rho_o \lambda_o)_{ij+1/2}^{t+1} T_{ij}^{t+1} (\psi_{oj}^{t+1} - \psi_{oi}^{t+1})] + (Vq_\text{o})_i^{t+1} = \frac{(V\phi\rho_\text{o} S_\text{o})_i^{t+1} - (V\phi\rho_\text{o} S_\text{o})_i^t}{\Delta t}, \quad (8)$$

$$\sum_{j \in N_i} [(\rho_{go} \lambda_o)_{ij+1/2}^{t+1} T_{ij}^{t+1} (\psi_{oj}^{t+1} - \psi_{oi}^{t+1}) + (\rho_g \lambda_g)_{ij+1/2}^{t+1} T_{ij}^{t+1} (\psi_{gj}^{t+1} - \psi_{gi}^{t+1})] + (Vq_g)_i^{t+1} = \frac{[V\phi(\rho_{go} S_o + \rho_g S_g)]_i^{t+1} - [V\phi(\rho_{go} S_o + \rho_g S_g)]_i^t}{\Delta t}, \quad (9)$$

$$\sum_{j \in N_i} [(\rho_w \lambda_w)_{ij+1/2}^{t+1} T_{ij}^{t+1} (\psi_{wj}^{t+1} - \psi_{wi}^{t+1})] + (Vq_w)_i^{t+1} = \frac{(V\phi\rho_w S_w)_i^{t+1} - (V\phi\rho_w S_w)_i^t}{\Delta t}, \quad (10)$$

where N_i denotes all the neighbors of gridblock i; superscript t denotes the previous time level; $t+1$ is the current time level; subscript $ij+1/2$ denotes upstream weighting of flow properties at the interface of gridblocks i and j; V_i is the volume of element i; Δt is the timestep size. The phase mobility λ is defined as

$$\lambda_\beta = k_{r\beta}/\mu_\beta. \quad (11)$$

T_{ij} is the transmissibility associated with the connection between gridblocks i and j, which is evaluated by two-point flux approximation (Lie 2014)

$$T_{ij} = \frac{T_i T_j}{T_i + T_j}, \quad (12)$$

where T_i is the one-sided transmissibility associated with block i, defined as

$$T_i = \frac{k_i A_{ij}}{d_i} \boldsymbol{n}_i \cdot \boldsymbol{c}_i, \quad (13)$$

where k_i is the absolute permeability of block i; A_{ij} is the interface area between gridblocks i and j; d_i is the distance between the centroid of block i and the centroid of the interface; $\boldsymbol{n}_i$ is the unit normal to the interface inside block i; $\boldsymbol{c}_i$ is the unit vector along the direction of the line joining the centroid of block i to the centroid of the interface. These quantities are illustrated in **Fig. 1.**

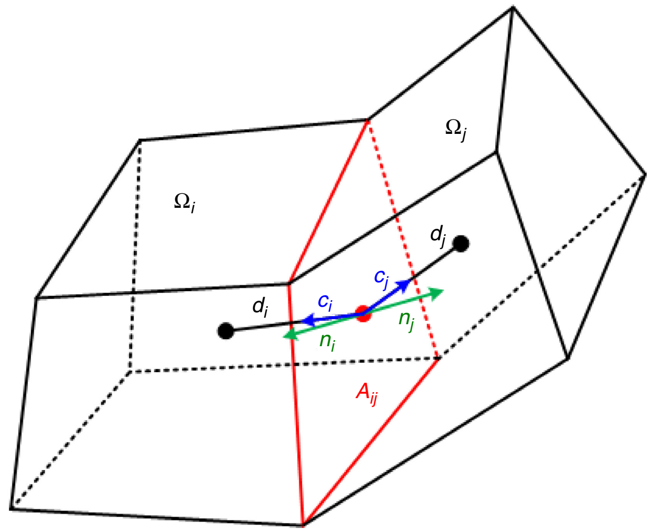

Fig. 1—Schematic of two adjacent blocks and the definition of different parameters involved in transmissibility.

The phase potential term $\psi_{\beta i}$ in Eqs. 8–10 is defined as

$$\psi_{\beta i} = p_{\beta i} - \rho_{\beta i} g D_i, \quad (14)$$

where D_i is the depth to the center of block i from a reference datum.

Then Eqs. 8–10 can be written in residual forms as follows

$$R_i^{o,t+1} = \frac{(V\phi\rho_o S_o)_i^{t+1} - (V\phi\rho_o S_o)_i^t}{\Delta t} - \sum_{j\in N_i}[(\rho_o\lambda_o)_{ij+1/2}^{t+1} T_{ij}^{t+1} \Delta_{ij}(\psi_o^{t+1})] - (Vq_o)_i^{t+1}, \quad (15)$$

$$R_i^{g,t+1} = \frac{[V\phi(\rho_{go}S_o + \rho_g S_g)]_i^{t+1} - [V\phi(\rho_{go}S_o + \rho_g S_g)]_i^t}{\Delta t} - \sum_{j\in N_i}[(\rho_{go}\lambda_o)_{ij+1/2}^{t+1} T_{ij}^{t+1} \Delta_{ij}(\psi_o^{t+1}) + (\rho_g\lambda_g)_{ij+1/2}^{t+1} T_{ij}^{t+1} \Delta_{ij}(\psi_g^{t+1})] - (Vq_g)_i^{t+1}, \quad (16)$$

$$R_i^{w,t+1} = \frac{(V\phi\rho_w S_w)_i^{t+1} - (V\phi\rho_w S_w)_i^t}{\Delta t} - \sum_{j\in N_i}[(\rho_w\lambda_w)_{ij+1/2}^{t+1} T_{ij}^{t+1} \Delta_{ij}(\psi_w^{t+1})] - (Vq_w)_i^{t+1}, \quad (17)$$

where the potential difference $\Delta_{ij}(\psi_\beta)$ can be calculated by

$$\Delta_{ij}(\psi_\beta) = p_{\beta j} - p_{\beta i} + \rho_{\beta,ij+1/2}(D_i - D_j)g. \quad (18)$$

For the above nonlinear equation system, the Newton–Raphson iteration method can be used and gives the following schemes

$$R_i^{\beta,t+1}(x_{k,p+1}) = R_i^{\beta,t+1}(x_{k,p}) + \sum_k \frac{\partial R_i^{\beta,t+1}(x_{k,p})}{\partial x_k}\delta x_{k,p+1} = 0, \quad (19)$$

$$\sum_k \frac{\partial R_i^{\beta,t+1}(x_{k,p})}{\partial x_k}\delta x_{k,p+1} = -R_i^{\beta,t+1}(x_{k,p}), \quad (20)$$

$$x_{k,p+1} = x_{k,p} + \delta x_{k,p+1}, \quad (21)$$

for $\beta = g, w,$ or o for gas, water and oil, respectively; where x_k is primary variable k with $k = 1$, 2, and 3 and p is iteration level. The Newton–Raphson iteration is conducted in one timestep, and the primary variables $x_{k,p+1}$ are updated until the residuals $R_i^{\beta,t+1}$, i.e., mass balance errors, over an iteration are reduced below preset convergence tolerances.

Modified EDFM. The EDFM is an efficient method to simulate complex fracture geometries. The reservoir can be discretized with flexible grid systems without consideration of the fractures. Then the fractures are embedded into the reservoir grid system, and discretized into fracture segments by the matrix block boundaries (Moinfar et al. 2014; Xu et al. 2017). A series of non-neighboring connections (NNC) and corresponding transmissibility are established to relate matrix and fracture systems. However, the discretization of fractures is actually highly sensitive to the matrix grid system and a quite complicated geometric problem, especially under 3D conditions. As shown in **Fig. 2,** various fracture segment shapes can be formed, such as triangular, quadrilateral, pentagonal, and hexagonal, even if the matrix grid is cuboid. More complexity may be introduced with complicated fracture geometries and matrix grid type, such as polygonal fractures and corner-point matrix grids.

It is clear that the difficulty is caused by the link of the fracture gridding with the matrix grid system. Therefore, it is natural to solve this problem by separating the fracture gridding process from the matrix grids. Then a modified EDFM is proposed here to simplify the discretization of 3D complex fracture geometries. In modified EDFM, the matrix and fractures are discretized separately. This results in two independent grid systems and greatly increases the flexibility of the meshing process. For example, structured grids or corner-point grids can be used for matrix discretization and unstructured grids for fractures, as shown in **Fig. 3.** Then the fracture grids are incorporated into the matrix grid systems in a way like the conventional EDFM.

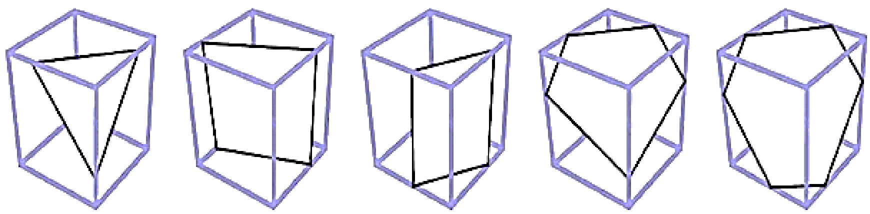

Fig. 2—Schematic of 3D fracture discretization in conventional EDFM.

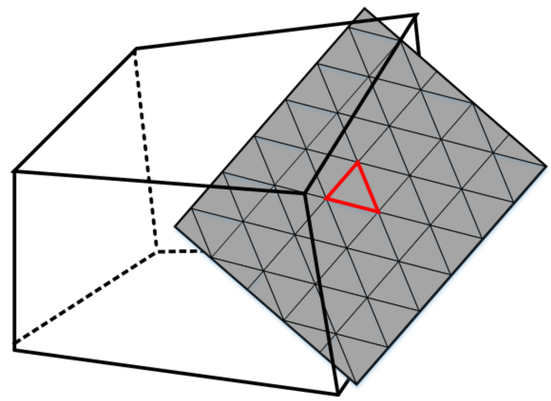

Fig. 3—Schematic of 3D fracture discretization in modified EDFM.

Similar to conventional EDFM, the key of modified EDFM is the calculation of NNC transmissibility. In the modified EDFM, there are two types of NNC transmissibility. One is the NNC transmissibility between fracture/matrix (*f–m*) grids, and another is the NNC transmissibility between fracture/fracture (*f–f*) grids.

The *f–m* transmissibility depends on the matrix permeability and fracture grid geometry. On the basis of the assumption that the pressure gradient in the matrix grid is uniform and normal to the fracture plane (Li and Lee 2008), the *f–m* transmissibility can be calculated by

$$T_{f-m} = \frac{2k_m A_f}{d_{f-m}}, \quad (22)$$

where A_f is the area of the fracture grid on one side; k_m is the matrix permeability; and $d_{f–m}$ is the average normal distance from matrix to the fracture grid, which is calculated as

$$d_{f-m} = \frac{\int |\boldsymbol{d} \cdot \boldsymbol{n}| \mathrm{d}V_m}{V_m}, \quad (23)$$

where V_m is the volume of the matrix gridblock; $\mathrm{d}V_m$ is the volume element of matrix; $\boldsymbol{d}$ is the vector from the volume element to the centroid of fracture grid; and $\boldsymbol{n}$ is the unit normal of the fracture plane. The integration in Eq. 23 may be difficult when the shape of matrix grid is irregular, such as corner-point grid shown in **Fig. 4a.** Here, the coordinate transformation is used to calculate the integration. As shown in Fig. 4, the corner-point grid is mapped into the reference grid, which is a cube with the length of each edge being two and has the center at the origin. The transformation functions, similar to the shape functions in finite element method, are defined in the reference grid to establish the mapping relation between the two grids as follows:

$$\boldsymbol{x}(\boldsymbol{\xi}) = \sum_{i=1}^{8} N_i(\boldsymbol{\xi})\boldsymbol{x}_i, \quad (24)$$

$$N_i(\boldsymbol{\xi}) = \frac{1}{8}(1 + \xi\xi_i)(1 + \eta\eta_i)(1 + \zeta\zeta_i), \quad (25)$$

where $\boldsymbol{x} = [x_1, x_2, x_3]^{\mathrm{T}}$ is the global coordinate; $\boldsymbol{\xi} = [\xi, \zeta, \eta]^{\mathrm{T}}$ is the reference coordinate; $N_i(\boldsymbol{\xi})$ is the interpolation function; $\boldsymbol{x}_i$ is the coordinate of node i; and (ξ_i, ζ_i, η_i) are the values of the reference coordinate corresponding to node i. Then Eq. 23 can be written as follows, and calculated by Gauss integration method as

$$d_{f-m} = \frac{\int_{-1}^{1}\int_{-1}^{1}\int_{-1}^{1} \tilde{\boldsymbol{d}}(\boldsymbol{\xi}) \cdot \tilde{\boldsymbol{n}} |\boldsymbol{J}| \mathrm{d}\xi \mathrm{d}\eta \mathrm{d}\zeta}{V_m} \approx \frac{\sum_{i=1}^{\mathrm{NG}} \omega_i \tilde{\boldsymbol{d}}(\boldsymbol{\xi}_i) \cdot \tilde{\boldsymbol{n}} |\boldsymbol{J}|}{V_m}, \quad (26)$$

where NG is the number of integration points; $\boldsymbol{\xi}_i$ is the integration point; ω_i is the integration weight; $\tilde{\boldsymbol{d}}(\boldsymbol{\xi})$ is the vector from (ξ, ζ, η) to the centroid of fracture grid in the reference coordinate; $\tilde{\boldsymbol{n}}$ is the transformed unit normal of the fracture plane; and $\boldsymbol{J}$ is the Jacobian matrix of the mapping, which can be obtained as follows:

$$\boldsymbol{J} = \frac{\partial \boldsymbol{x}}{\partial \boldsymbol{\xi}} = \sum_{i=1}^{8} \boldsymbol{x}_i \frac{\partial N_i(\boldsymbol{\xi})}{\partial \boldsymbol{\xi}}. \quad (27)$$

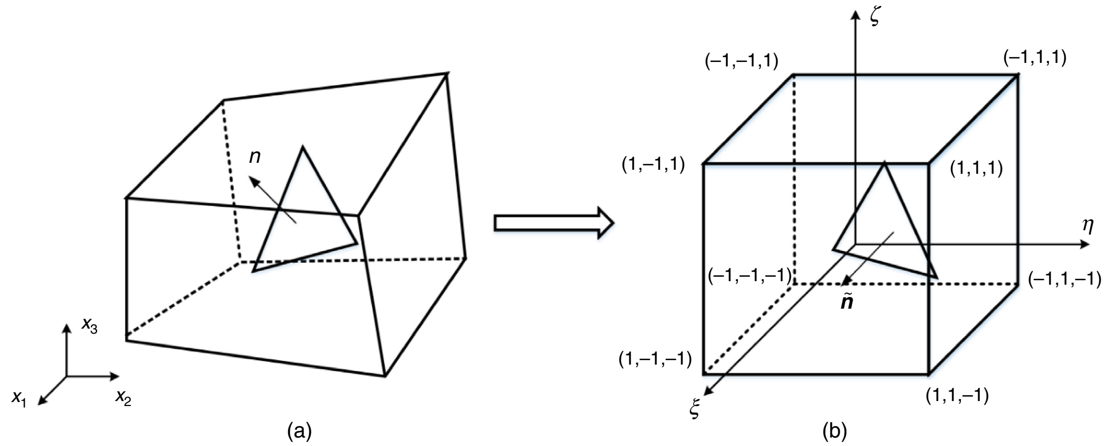

Fig. 4—Schematic of coordinate transformation from (a) corner-point grid to (b) reference grid.

Moreover, it should be noted that the coordinate transformation shown in Fig. 4 is only used to calculate the integration in Eq. 23. The phase potential and the flux calculation are still evaluated in the original space.

However, when a fracture grid is located at matrix grid boundaries, as the red fracture grid shown in Fig. 3, the calculation of the interface area between the matrix and fracture grids may involve 3D plane intersection problem. For simplicity, only the connection between the fracture grid and the matrix gridblock where the centroid of fracture grid is located is evaluated. The *f–m* transmissibility is calculated by Eq. 22 using the whole area of fracture grid as the interface area between the matrix and fracture grids. Errors can be introduced by this approximation, but reduced by using small-size fracture grids, commonly comparable to or smaller than matrix grid, which are evidenced by the results in the Validation of modified EDFM subsection.

The *f–f* transmissibility includes the transmissibility between fracture grids in one individual fracture, and intersected fracture grids in different fractures, as shown in **Fig. 5.** For the fracture grids in one individual fracture, only involving the connections between two fracture grids as the blue grids in Fig. 5, the *f–f* transmissibility can be normally calculated in a way like Eq. 12

$$T_{f-f} = \frac{\alpha_1 \alpha_2}{\alpha_1 + \alpha_2}, \quad (28)$$

$$\alpha_i = \frac{A_i k_i}{d_i} \boldsymbol{n}_i \cdot \boldsymbol{f}_i, \quad (29)$$

where A_i is the area of the interface between the two fracture grids; k_i is the permeability of fracture grid i; d_i is the distance between the centroid of the interface and the centroid of fracture grid i; $\boldsymbol{n}_i$ is the unit normal to the interface inside fracture grid i; and $\boldsymbol{f}_i$ is the unit vector along the direction from the centroid of the interface to the centroid of fracture grid i.

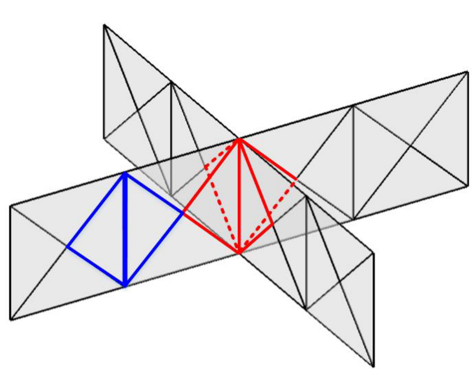

Fig. 5—Schematic of fracture grids for calculation of fracture transmissibility. The blue grids represent the fracture grids in one individual fracture, and the red ones represent the grids at fracture intersection.

For the fracture grids at fracture intersections, the connections among multiple fracture grids (commonly more than two grids) are involved, such as the red grids in Fig. 5. To evaluate the transmissibility at fracture intersections, the approximation, i.e., star-delta transformation, proposed by Karimi-Fard et al. (2004) is adopted. For an intersection with n connections, the *f–f* transmissibility can be calculated by

$$T_{i-j} = \frac{\alpha_i \alpha_j}{\sum_{k=1}^{n} \alpha_k}, \quad (30)$$

where T_{i-j} is the transmissibility between fracture grids i and j, and the calculation of α_k can refer to Eq. 29.

Vug Model. In vugs or karst conduits, the fluid flow usually exhibits free flow regime and follows Navier–Stokes equation. Therefore, porous flow and free flow coexist in fractured vuggy reservoirs. However, the coupling system of porous and free flow is very complicated, and its numerical solution also remains challenging especially under multiphase flow condition.

To meet the demands of engineering application, a simplified vug model is proposed on the basis of some reasonable assumptions. In this model, we assume a low-velocity laminar flow in vugs, and then the instantaneous gravity differentiation is assumed for the multiphase fluids, which will be separated vertically with clear phase interfaces according to their densities. It should be noted that the assumption is basically valid due to the low velocity of underground fluid unless there are wells producing or injecting on the vugs with high flow rate.

On the basis of the proposed vug model, the whole vug region can be treated as one gridblock. As shown in **Fig. 6,** the irregular vug, together with matrix, is firstly discretized into a series of subgrids. The vug gridblock can be obtained by merging the subgrids locating in the vug region. Then the volume of the vug gridblock can be calculated by

$$V_v = \sum_n V_n, \quad (31)$$

where V_v and V_n denote the volumes of vug gridblock and subgrid n. Moreover, the governing equations and numerical formulations 1–10 are also applicable for the vug model, but the transmissibility and phase mobility are calculated by

$$T_{v-m} \approx T_m = \frac{A_m k_m}{d_m} \boldsymbol{n}_m \cdot \boldsymbol{c}_m, \quad (32)$$

$$\lambda_\beta = \tilde{k}_{r\beta} / \mu_\beta, \quad (33)$$

where $T_{v\text{–}m}$ is the vug/matrix transmissibility, which is approximate to the one-sided transmissibility of matrix block T_m because of the high conductivity of vugs; A_m is the interface area between vug and matrix gridblocks; d_m is the distance between the centroid of interface and centroid of matrix gridblock; $\boldsymbol{n}_m$ is the unit normal to the interface inside matrix gridblock; and $\boldsymbol{c}_m$ is the unit vector along the direction from the centroid of the interface to the centroid of matrix gridblock. Similarly, the vug/fracture transmissibility $T_{v\text{–}f}$ can be approximate to the one-sided transmissibility of fracture block T_f. In addition, there are two notable points: one is that the vug pressure needs to be evaluated at the depth of its neighboring grid according to the pressure at the centroid of the vug gridblock and the phase distribution in vug, when calculating the potential difference between vug and its neighboring grids. The other is that the phase density ρ_β and relative permeability $\tilde{k}_{r\beta}$ are still determined by the upstream weighting method, but $\tilde{k}_{r\beta}$ needs to be redefined. As shown in Fig. 6, when the fluid flow direction is from matrix to vug, ρ_β and $\tilde{k}_{r\beta}$ take the phase density and relative permeability of matrix gridblock. Reversely, ρ_β takes the phase density of vug gridblock, but $\tilde{k}_{r\beta}$ takes the phase flow fraction, which is a newly defined variable closely related to the relative location between vug and matrix/fracture grids, and the saturation in vug gridblock.

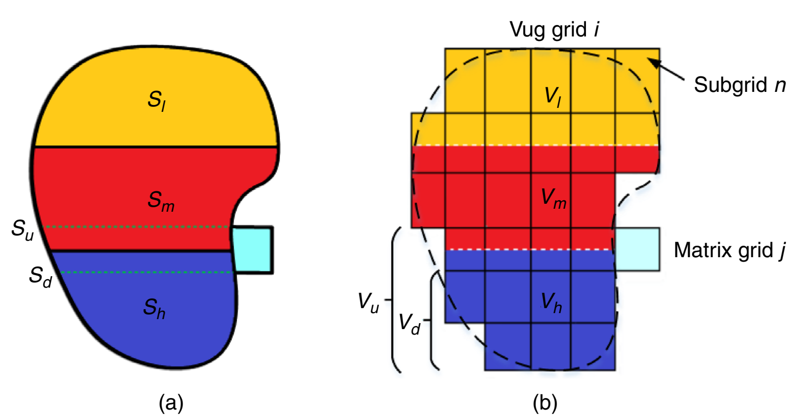

Fig. 6—Schematic of (a) simplified vug model and (b) vug gridblock.

As shown in Fig. 6, we assume a three-phase flow in the vug/matrix system. Because the curved surface of the vug is replaced with a series of planes, the phase flow fraction $\tilde{k}_{r\beta}$ can be written as following linear forms

$$S_h \le S_d \Rightarrow \begin{bmatrix} S_h + S_m \le S_d \Rightarrow \tilde{k}_{rl} = 1, \tilde{k}_{rm} = 0, \tilde{k}_{rh} = 0 \quad (l) \\ S_d < S_h + S_m \le S_u \Rightarrow \tilde{k}_{rl} = 1 - \tilde{k}_{rm}, \tilde{k}_{rm} = \dfrac{S_h + S_m - S_d}{S_u - S_d}, \tilde{k}_{rh} = 0 \quad (l-m) \\ S_h + S_m > S_u \Rightarrow \tilde{k}_{rl} = 0, \tilde{k}_{rm} = 1, \tilde{k}_{rh} = 0 \quad (m) \end{bmatrix},$$

$$S_d < S_h \le S_u \Rightarrow \begin{bmatrix} S_d < S_h + S_m < S_u \Rightarrow \tilde{k}_{rl} = 1 - \tilde{k}_{rm} - \tilde{k}_{rh}, \tilde{k}_{rm} = \dfrac{S_m}{S_u - S_d}, \tilde{k}_{rh} = \dfrac{S_h - S_d}{S_u - S_d} \quad (l-m-h) \\ S_h + S_m > S_u \Rightarrow \tilde{k}_{rl} = 0, \tilde{k}_{rm} = 1 - \tilde{k}_{rh}, \tilde{k}_{rh} = \dfrac{S_h - S_d}{S_u - S_d} \quad (m-h) \end{bmatrix},$$

$$S_h > S_u \Rightarrow \tilde{k}_{rl} = 0, \tilde{k}_{rm} = 0, \tilde{k}_{rh} = 1 \quad (h), \quad (34)$$

where S_l, S_m, and S_h denote the saturations of light, medium, and heavy phase fluids in vug gridblock, which depend on the phase density; S_u and S_d are the saturations corresponding to the upper and lower bounds of the matrix gridblock, which can be calculated by

$$S_u = \frac{V_u}{V_v}, \quad (35)$$

$$S_d = \frac{V_d}{V_v}, \quad (36)$$

where V_u and V_d are volumes corresponding to the S_u and S_d, which can be obtained by summing the volumes of subgrids below the lower and upper bounds of the matrix gridblock, as shown in Fig. 6.

It is clear that Eq. 34 gives all possible conditions from single-phase to three-phase flow. However, it should be noted that $\tilde{k}_{r\beta}$ is different for different matrix gridblocks due to the different relative locations between vug and matrix gridblocks. The preprocessing of $\tilde{k}_{r\beta}$ needs to be done before the simulation.

Model Validation

This section is divided into two subsections. The first part is the modified EDFM, and the second part is the vug model.

Validation of Modified EDFM. As shown in **Fig. 7**, a 3D reservoir model with two intersected vertical fractures is designed to validate the modified EDFM. The model dimension is $110 \times 110 \times 50$ m. The basic reservoir and fracture properties are listed in **Table 1.** The water/oil relative permeability curves for matrix and fracture are shown in **Fig. 8,** and the capillary pressure and fluid compressibility are not included. Then the water/oil two-phase flow simulations are conducted with conventional and modified EDFM, and the results of conventional EDFM are taken as the reference. The grid systems of these two models, with the same characteristic matrix grid size of 5 m, are shown in **Fig. 9.** Besides, due to the independence of the matrix and fracture grid system in modified EDFM, the fracture grid sensitivity is also conducted with different characteristic fracture grid sizes of 6, 4, and 2 m. The number of generated fracture grids for conventional EDFM and the three modified EDFM cases are 370, 656, 1,382, and 5,018, and the computational times on a single processor are 340.2, 391.8, 470.1, and 703.2 seconds, respectively.

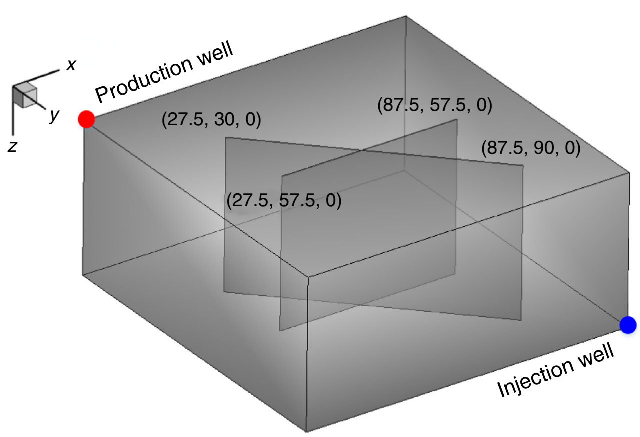

Fig. 7—Schematic of the reservoir model for validation of modified EDFM.

Parameter	Value	Unit
Matrix porosity	0.1	–
Matrix permeability	1	md
Fracture aperture	0.01	m
Fracture permeability	10^4	md
Matrix compressibility	7.25×10^{-3}	MPa^{-1}
Fracture compressibility	2×10^{-2}	MPa^{-1}
Initial reservoir pressure	30	MPa
Initial water saturation	0.2	–
Production bottomhole pressure	20	MPa
Injection bottomhole pressure	40	MPa
Wellbore radius	0.1	m
Oil viscosity	2.17	mPa·s
Water viscosity	1	mPa·s

Table 1—Basic reservoir parameters.

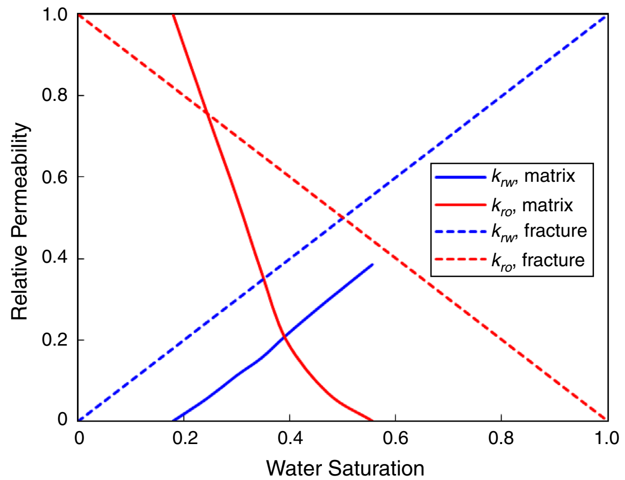

Fig. 8—Water/oil relative permeability curves for matrix and fractures.

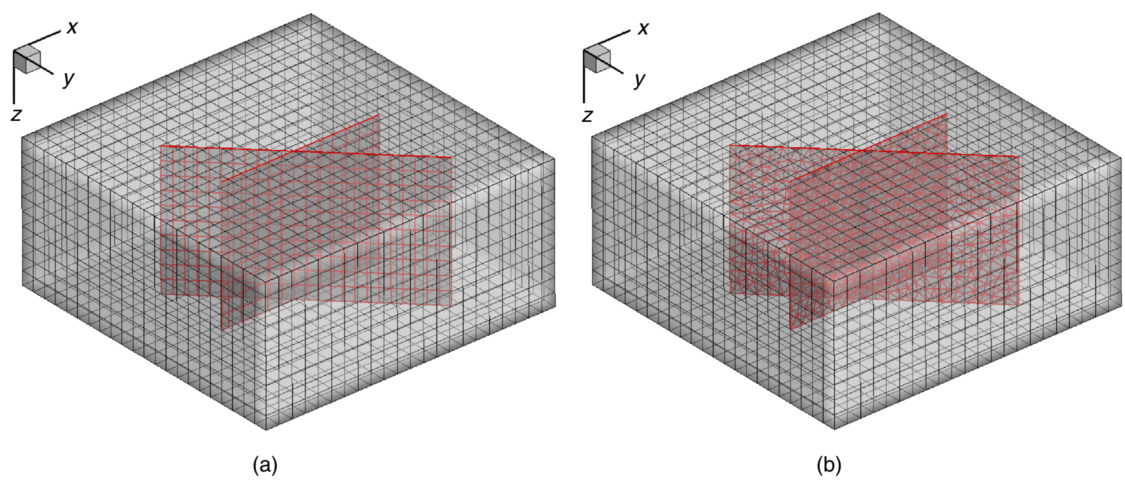

Fig. 9—Grid systems for (a) conventional EDFM and (b) modified EDFM.

Fig. 10 shows the matrix pressure and saturation distribution on the line from (2.5, 57.5, 22.5) to (107.5, 57.5, 22.5) after 2,000 days of production. We can see that the pressure results of the modified EDFM fits well with the reference. However, some deviations exist on the oil saturation and become larger with the increase of fracture grid size. This can be explained by **Fig. 11,** where the pressure distribution on the fractures is not sensitive to fracture grid size, but the saturation is. This is because with the increase of fracture size, one fracture grid can cross several matrix grids but only connect with the matrix grid where the center of fracture grid locates. Then the fluid exchange of different phases between matrix and fracture grids can be overestimated, which can cause local saturation perturbation. Different from the extremely time-dependent saturation field, the pressure distribution, smoothly decreasing from injection well to production well, is much less sensitive to fracture grid size. To further investigate the errors caused by the approximation of interface area between matrix and fracture grids, the pressure and saturation evolutions in the matrix grid locating at (87.5, 87.5, 22.5) are provided in **Fig. 12.** The results of modified EDFM fit well with those of conventional EDFM, in which the average relative errors for pressure and saturation are all below 1% with fracture grid size being 2, 4, and 6 m. Moreover, **Fig. 13** gives the oil and water production rates over 2,000 days, which shows good agreements among these four cases and confirms the accuracy of modified EDFM.

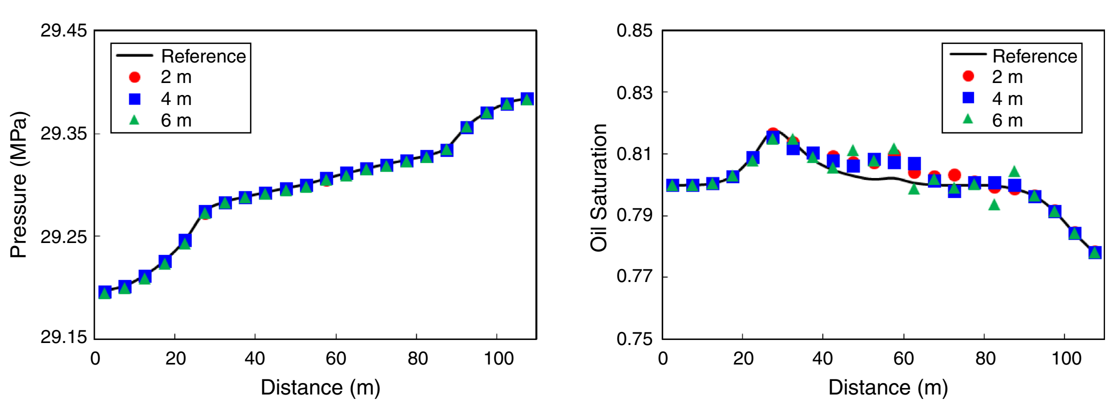

Fig. 10—Comparison of (a) pressure and (b) oil saturation on the line from (2.5, 57.5, 22.5) to (107.5, 57.5, 22.5) between conventional EDFM (reference) and modified EDFM after 2,000 days of production.

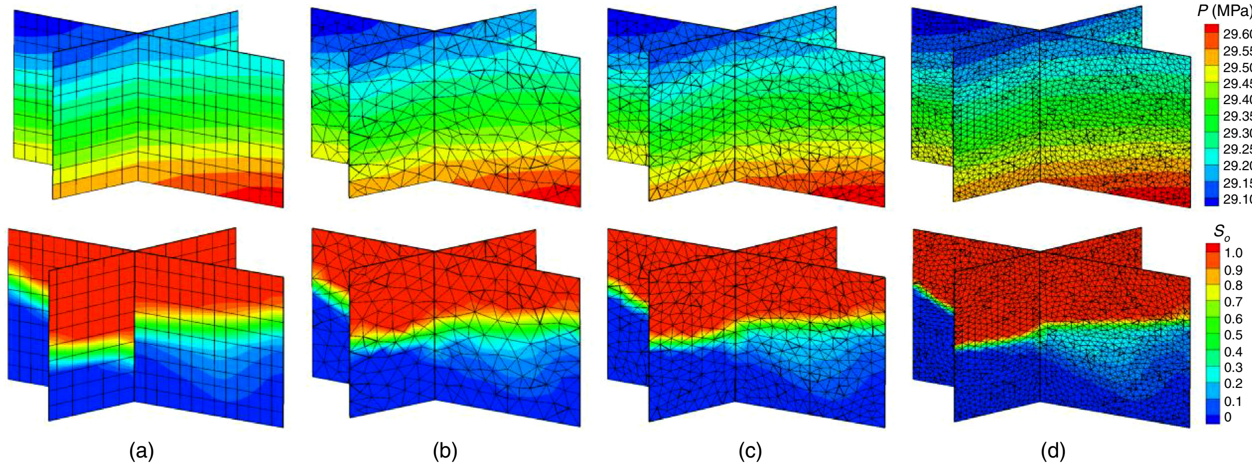

Fig. 11—Comparison of pressure and oil saturation in fractures calculated by (a) conventional EDFM (reference) and modified EDFM with different fracture grid sizes of (b) 6 m, (c) 4 m, and (d) 2 m after 2,000 days of production.

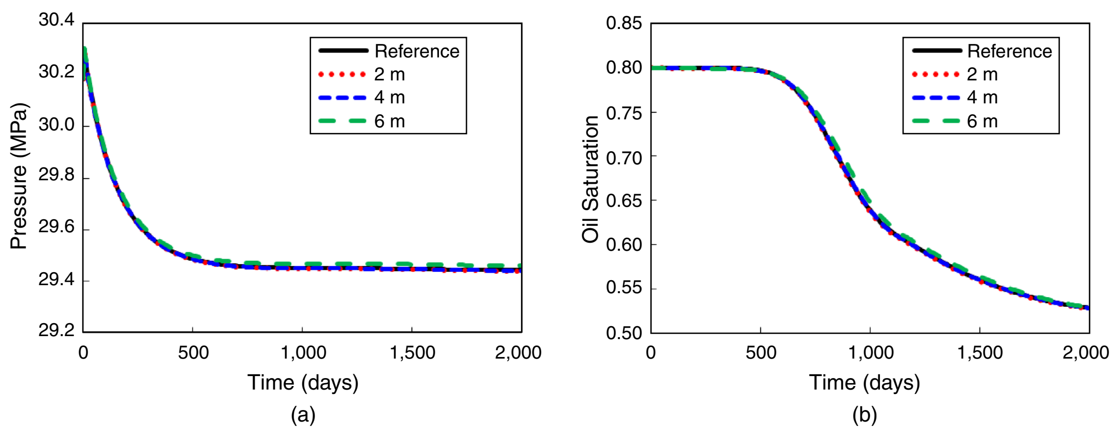

Fig. 12—Comparison of (a) pressure and (b) oil saturation evolution in the matrix grid locating at (87.5, 87.5, and 22.5) between conventional EDFM (reference) and modified EDFM over 2,000 days of production.

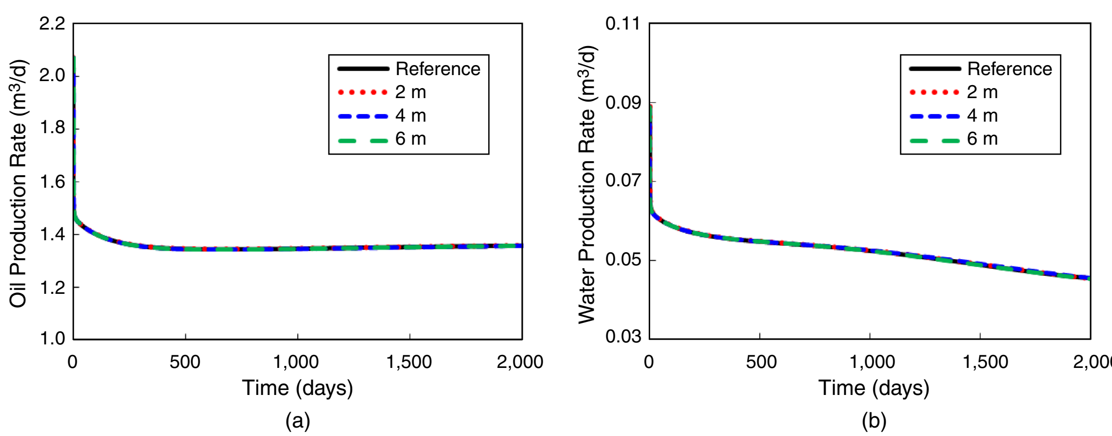

Fig. 13—Comparison of (a) oil and (b) water production rates over 2,000 days of production calculated by conventional EDFM (reference) and modified EDFM with fracture grid sizes of 6, 4, and 2 m.

Validation of Vug Model. A simple conceptual model is designed for the validation of the proposed vug model, as shown in **Fig. 14.** In the model, two same-sized vugs are connected with three fractures. The dimension of the vug is 20×30 mm. The aperture of the fractures is 1 mm, and the length is 5 mm. The fluid properties in Table 1 are used. An injection well is located on the left fracture with a constant injection rate of 0.144 m^3/d, and a production well is placed on the right fracture. S_u and S_d can be calculated according to Eqs. 34 and 35, which are (0.1333, 0.1667), (0.4667, 0.5), and (0.8, 0.8333) for the three fractures from left to right. Then a water/oil two-phase flow simulation, on the basis of the proposed vug model and VOF method, are both conducted on the vug model. The results of VOF are taken as the reference. **Fig. 15** shows the oil saturation results of VOF at 0.048 hours and 0.134 hours when water starts to get into the latter two fractures. It is obvious that the water and oil have been separated with a clear interface, which verifies the assumption of instantaneous gravity differentiation. A further proof of the agreement between the results of the two simulations is provided in **Fig. 16.**

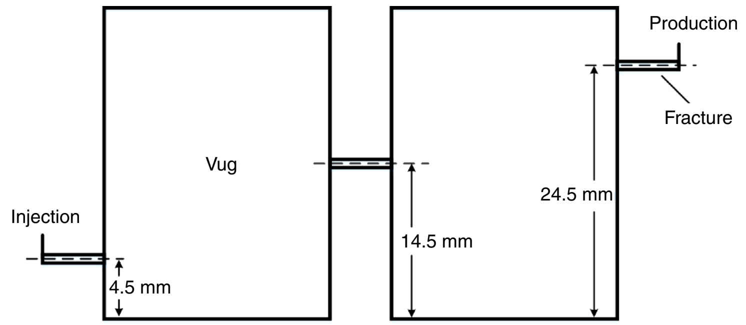

Fig. 14—Conceptual model for validation of vug model with two same-sized vugs and three fractures.

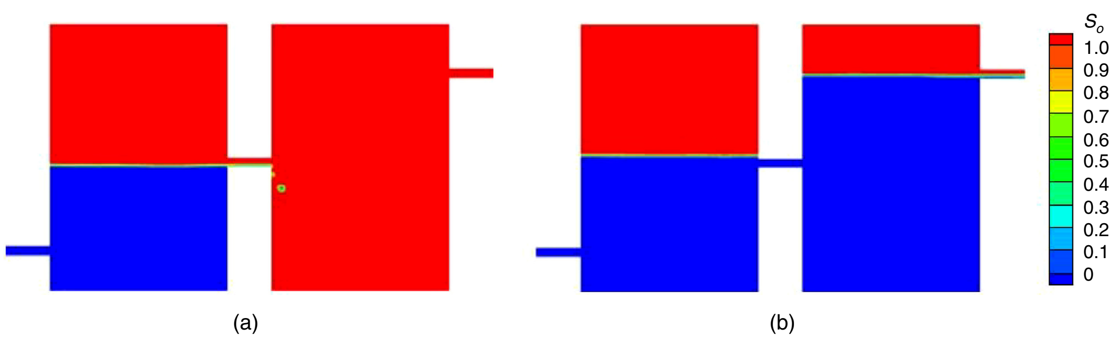

Fig. 15—Oil saturation distribution results of VOF method at (a) 0.048 hours and (b) 0.134 hours when the water starts to flow into the latter two fractures.

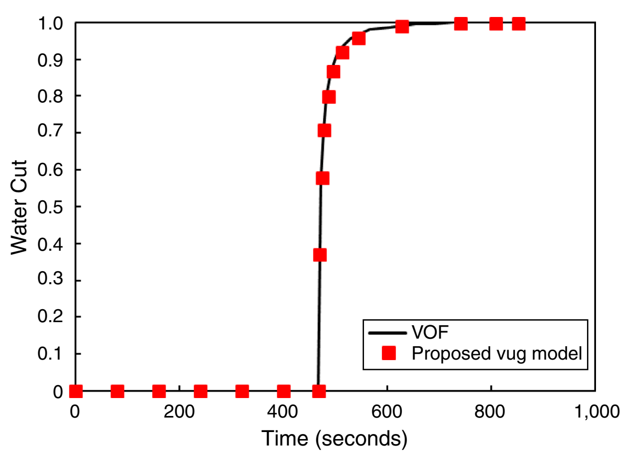

Fig. 16—Comparison of water cut calculated by the proposed vug model and VOF.

Results and Discussions

In this section, we focus on the application of the proposed hybrid model. Three typical fracture-vug unit models are designed to investigate the effect of fracture-vug configuration on the flow and production performance. Then a real oilfield model is used to test the practicability of the hybrid model in complex geological model.

Typical Fracture-Vug Unit Model. In fractured vuggy reservoirs, various local fracture and vug configurations are distributed (Loucks 1999). Among these configurations, several typical fracture-vug unit models can be summarized. The flow and production performance may be greatly different when the injection and production wells are placed on different fracture-vug units. Therefore, it is necessary to understand the flow and production characters of different fracture-vug units, which can give us some insights into the reservoir production responses. **Fig. 17** shows a schematic of fractured vuggy reservoir, in which three typical fracture-vug units are contained: fracture unit, fracture-isolated vug unit, and fracture-karst conduit unit. To investigate the production performance of different typical fracture-vug units, the corresponding three typical fracture-vug units are designed with the production and injection wells placing at two opposite corners as shown in **Fig. 18.** The dimension of the three models is $110 \times 110 \times 50$ m. The fluid and reservoir properties in Table 1, as well as the relative permeability curve in Fig. 8 are used here.

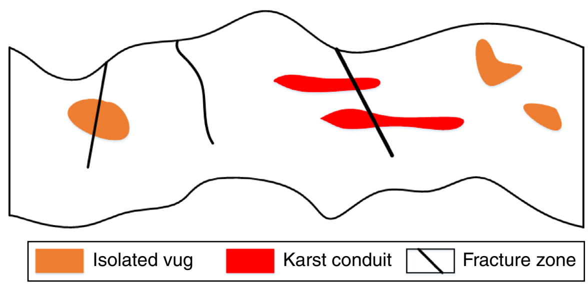

Fig. 17—Schematic of fractured vuggy reservoir with several typical fracture-vug units.

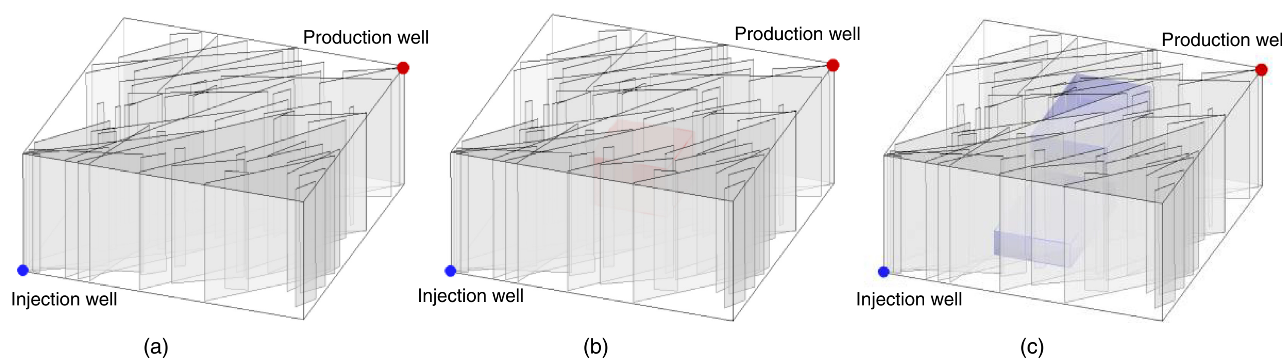

Fig. 18—Physical models for three typical fracture-vug units of (a) fracture unit, (b) fracture-isolated vug unit, and (c) fracture-karst conduit unit.

To obtain reliable results, a grid-sensitivity study is firstly performed on the basis of the case (a) in Fig. 18. Besides, the simulations are conducted using conventional EDFM and modified EDFM, respectively, to further validate the accuracy of modified EDFM. Three simulation cases with $33 \times 33 \times 10$, $55 \times 55 \times 10$, and $77 \times 77 \times 10$ matrix grids are designed, and the corresponding fracture grid sizes are 3.3, 2, and 1.4 m in modified EDFM. **Fig. 19** shows the matrix and fracture grids used in conventional EDFM and modified EDFM. **Fig. 20** shows comparisons of the water saturation distribution in matrix and fractures, and the results of oil production rate after 2,000 days of production are shown in **Fig. 21.** As can be seen, the stable water saturation distribution, as well as oil production profile, can be obtained when the grid number reaches $55 \times 55 \times 10$. Moreover, the good agreements between the results of conventional EDFM and modified EDFM further verify the accuracy of the proposed modified EDFM. The simulation performances of modified EDFM and conventional EDFM are summarized in **Table 2.** The significant increase of computation time for modified EDFM is mainly attributed to the increase of fracture grid number. Besides, the direct linear solver used in our in-house simulator can also lead to the significant increase of computational time with the increase of grid number. Although the computational cost is larger for modified EDFM, the fracture meshing process is more flexible comparing with conventional EDFM, which avoids the complicated 3D structure intersection problems.

On the basis of the results of grid-sensitivity study, the number of matrix grids is set as $55 \times 55 \times 10$ (before the subgrids are merged into vug gridblocks), and the fracture grid size is set as 2 m in cases (b) and (c). **Fig. 22** shows the oil saturation in matrix and fractures in the three units after 2,000 days of production, and the oil production rate and water-cut curves are shown in **Fig. 23.** As shown in Fig. 22a, it is clear that because of the good connectivity and high conductivity of fractures, the injected water breaks through quickly in the fractures, leading to the quick increase of water cut in the fracture unit. Then compared with Fig. 22b and the production profiles of the fracture-isolated vug unit in Fig. 23, we can see that the isolated vug promotes the water breakthrough as a result of the injected water in the vug segregating from oil and settling to the bottom of the vug. Then through the fractures on the side of the vug, the water will get into the production well soon. Therefore, the isolated vug actually decreases the traveling path of the injected water. Finally, the production profiles of the fracture-karst conduit unit show more stable oil production rate and slower water-cut increase than the other two cases. This is common in real fractured vuggy reservoirs, which is mainly caused by the storage effect of karst conduits and the interactions between the two karst conduits. When the water gets into the lower conduit, the water will be segregated and located at the bottom. Then the upper conduit can hinder the water breakthrough unless the water reaches to the top of the lower conduit, which is evidenced by the saturation distribution in fractures, as well as the second and third layers of matrix, as shown in Fig. 22c. From the results of the three models, it is clear that the production performance is greatly influenced by the local fracture and vug configuration. Moreover, it should be noted that the effect of vugs and karst conduits can be more complex in reality, which depends on the location of vugs and karst conduits, as well as their interactions.

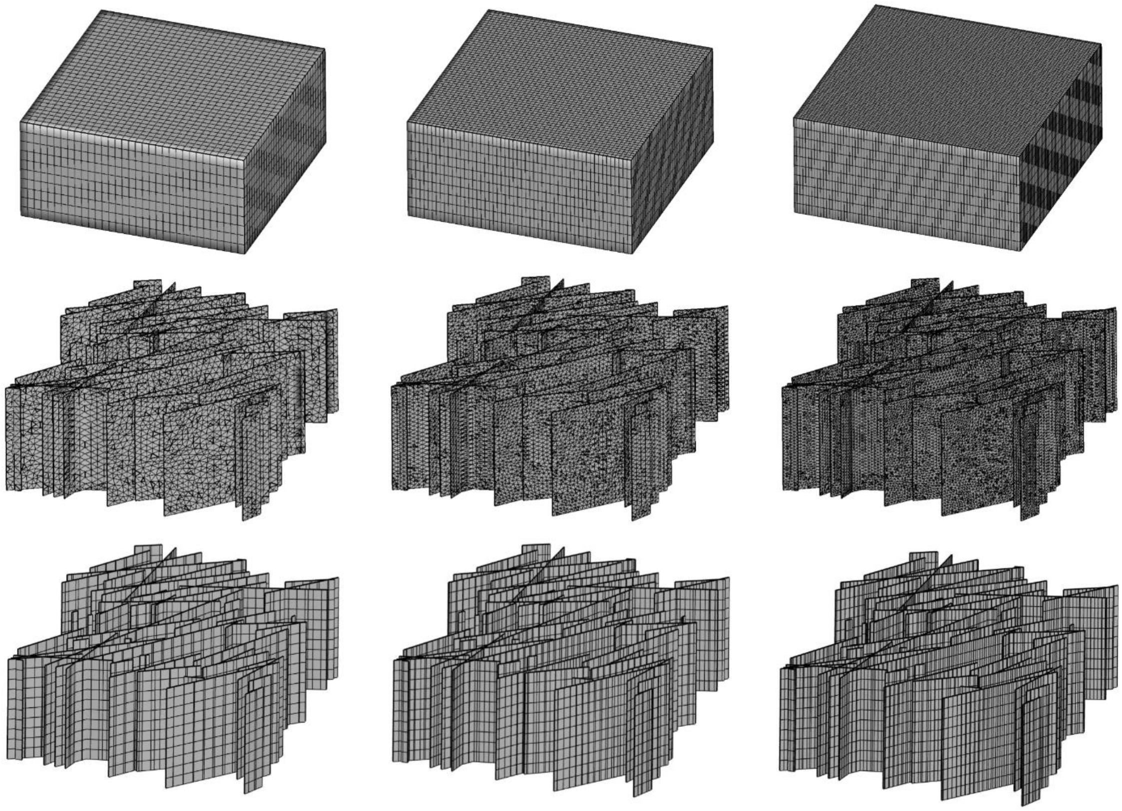

Fig. 19—Matrix and fracture grids for the grid-sensitivity study performed on the case (a) in Fig. 18—The fracture grids in the second row are used for modified EDFM, and those in the third row are used for conventional EDFM. The matrix grid number is 33 × 33 × 10, 55 × 55 × 10, and 77 × 77 × 10, and the fracture characteristic grid size is 3.3, 2, and 1.4 m for (a)–(c) cases with different resolutions.

Tahe Oilfield Model. Real fractured vuggy reservoir models usually have very complex geologic structures and complicated fracture and vug geometries. Because of the complexity of structures, the corner-point grid is commonly used in the geologic modeling. However, the fractures and vugs are typically represented by simple techniques, such as equivalent methods. Therefore, there is a need to improve the modeling of fractures and vugs. Here, our proposed modified EDFM and vug models are applied to simulate a Tahe Oilfield Model, a real fractured vuggy reservoir in western China, with complicated fracture and vug geometries. The objective is to demonstrate that the proposed model is sufficiently flexible to handle the complicated real field problems. Meanwhile, on the basis of the real reservoir model, the history matching is carried out to further validate the proposed models.

Fig. 24 shows the geologic matrix and fracture geometries of the Tahe Oilfield Model. The model consists of 21 wells and 136 fractures, and the bottomwater is considered located at the bottom of the reservoir. The geological model is discretized into 754,371 corner-point grids with 239,629 active grids, and the fracture model is discretized into 38,770 grids. By use of the grid process function of the MATLAB® reservoir simulation toolbox (MRST; The Mathworks, Inc., Natick, Massachusetts, USA; Lie 2014), the inactive grids are removed, and the grid information for flow simulation is calculated. **Fig. 25** shows the active matrix and fracture grid systems. Then the history matching is conducted with the daily liquid production rates specified for production wells and water injection rates specified for injection wells. **Fig. 26** shows the pressure and oil saturation distributions in matrix and fractures after 2,500 days of production. **Fig. 27** shows the comparisons of oil production rate and water-cut for two representative wells between history production data and simulation results, and **Fig. 28** shows the results of water-cut for the whole reservoir. As can be seen, the simulation results of oil production rate and water-cut for the two representative wells fit well with the history data, and the water-cut for the whole reservoir also shows similar trends. Moreover, the rapid increase of water-cut at the late stage is well captured by considering the effect of bottomwater.

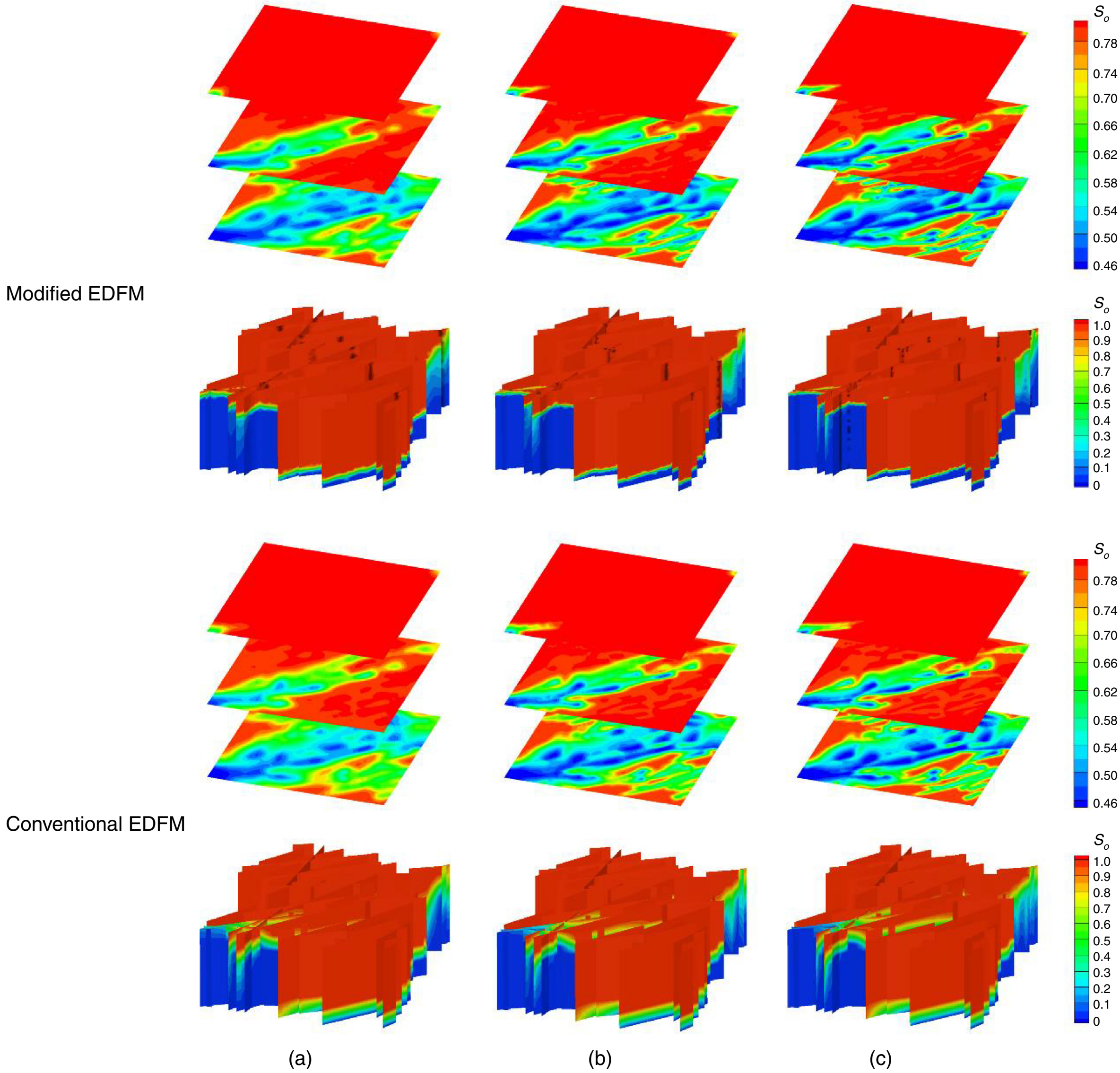

Fig. 20—Oil saturation distribution in matrix and fractures calculated by modified EDFM (first two rows) and conventional EDFM (last two rows) after 2,000 days of production. The results of different resolutions corresponding to the cases in Fig. 19 are shown in different columns. For matrix, the water saturation in three layers (top, middle, and bottom layers) is shown.

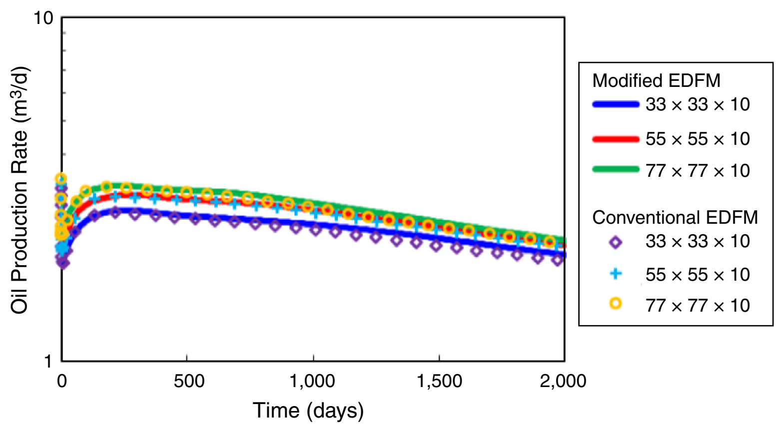

Fig. 21—Comparison of oil production rate calculated by conventional EDFM and modified EDFM under different resolutions.

	Matrix Grid Number	Number of Timesteps	Number of Newton Iterations	CPU Time (minutes)
Conventional EDFM	33 × 33 × 10	219	1,423	69
	55 × 55 × 10	225	1,831	318
	77 × 77 × 10	218	1,825	715
Modified EDFM	33 × 33 × 10	223	1,562	365
	55 × 55 × 10	242	1,928	716
	77 × 77 × 10	221	1,886	1534

Table 2—Simulation performance of modified EDFM and conventional EDFM. CPU = central processing unit.

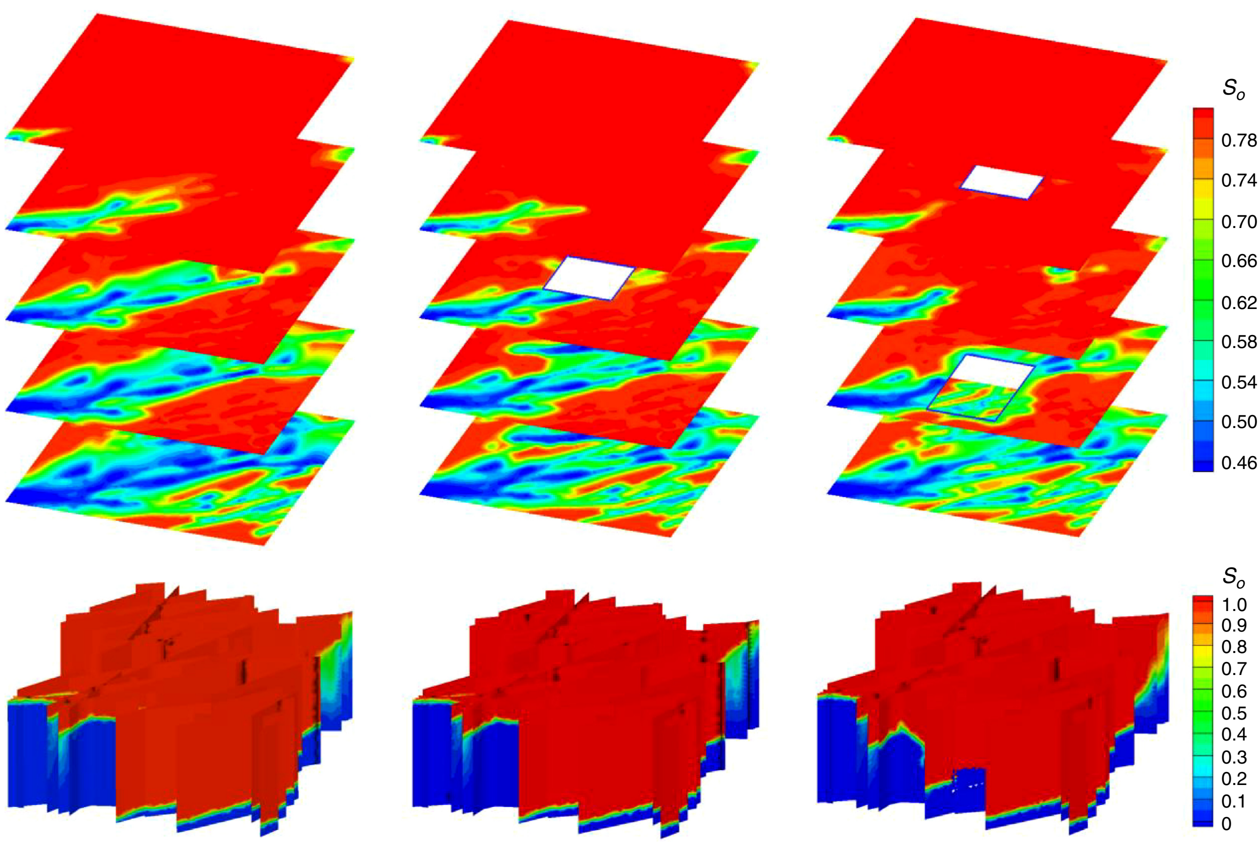

Fig. 22—Oil saturation distribution in matrix (fist row) and fractures (second row) in (a) fracture unit, (b) fracture-isolated vug unit, and (c) fracture-karst conduit unit after 2,000 days of production.

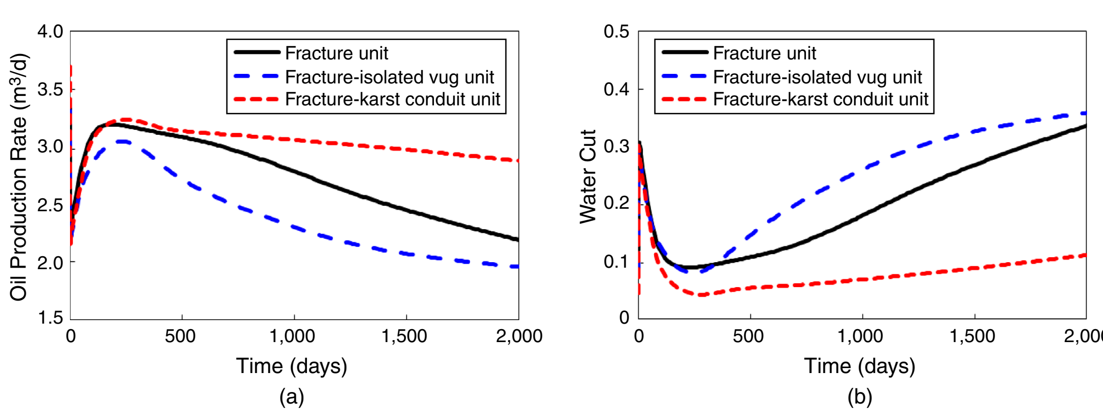

Fig. 23—(a) Oil production rate and (b) water-cut curves of different typical fracture-vug units.

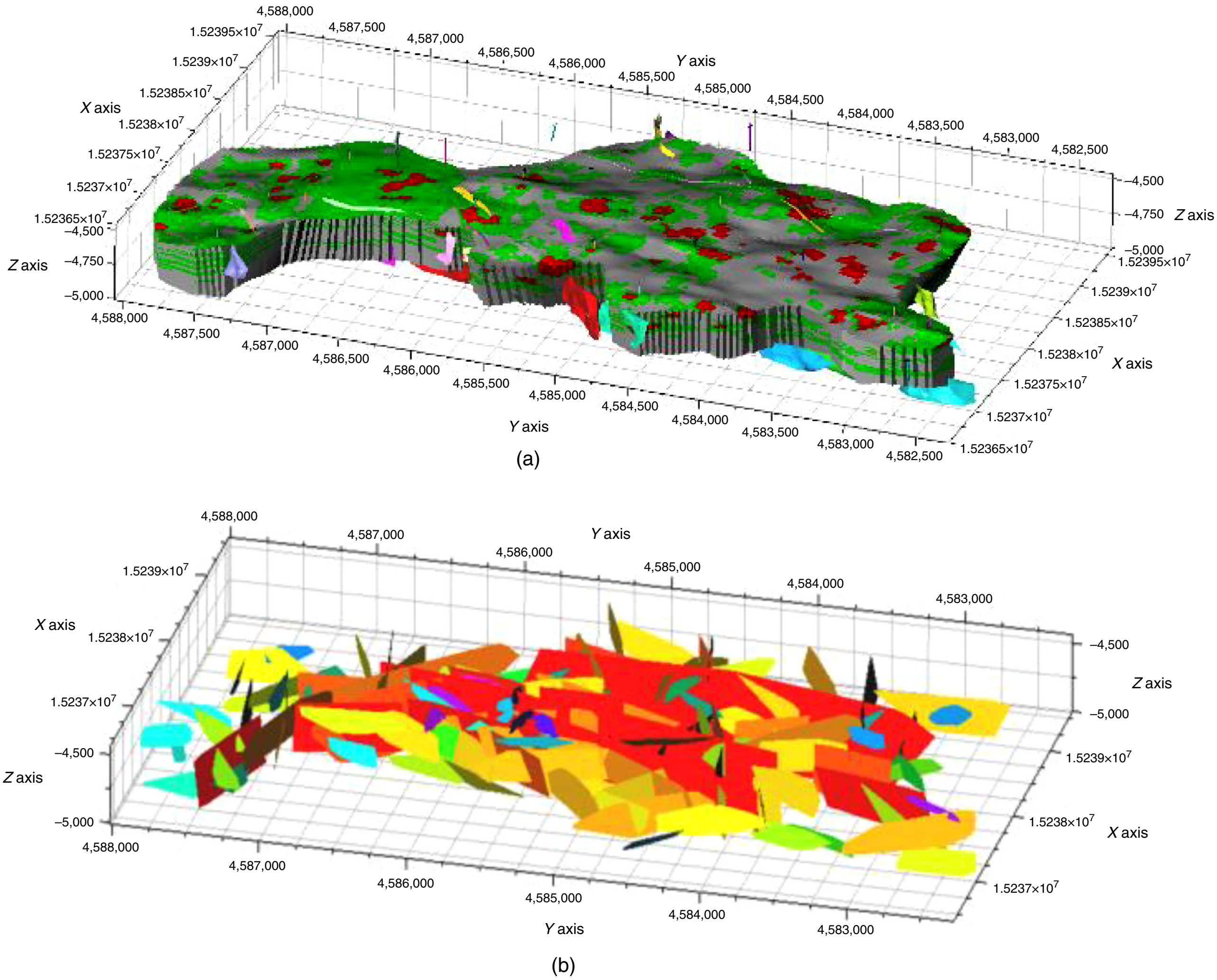

Fig. 24—(a) Geologic model with vugs (red), active matrix (green), inactive matrix (gray), and faults (colorful surfaces) and (b) fracture geometries of a Tahe Oilfield Model.

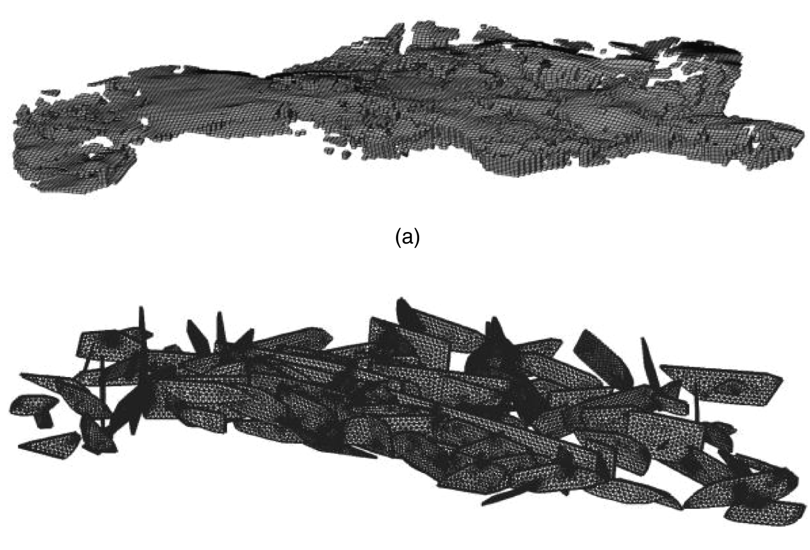

Fig. 25—Grid systems for (a) matrix and (b) fractures.

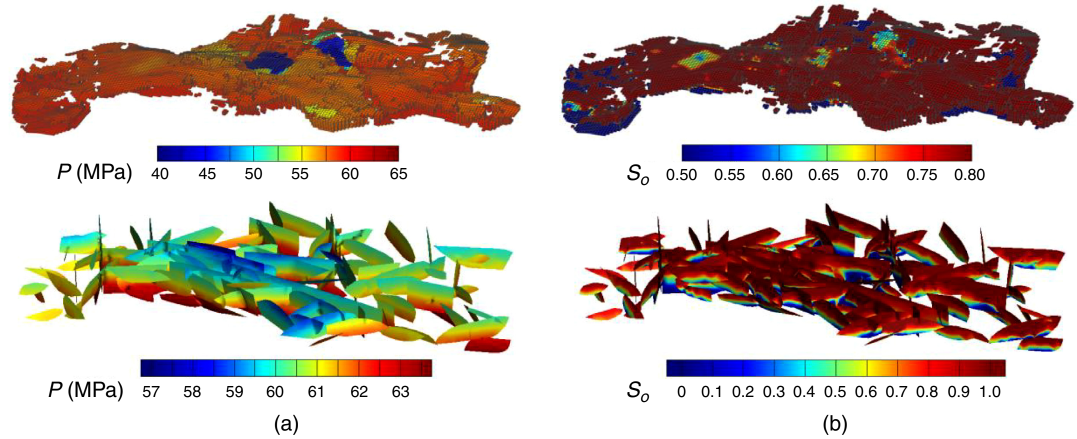

Fig. 26—(a) Pressure and (b) oil saturation distribution in matrix (first row) and fractures (second row) after 2,500 days of production.

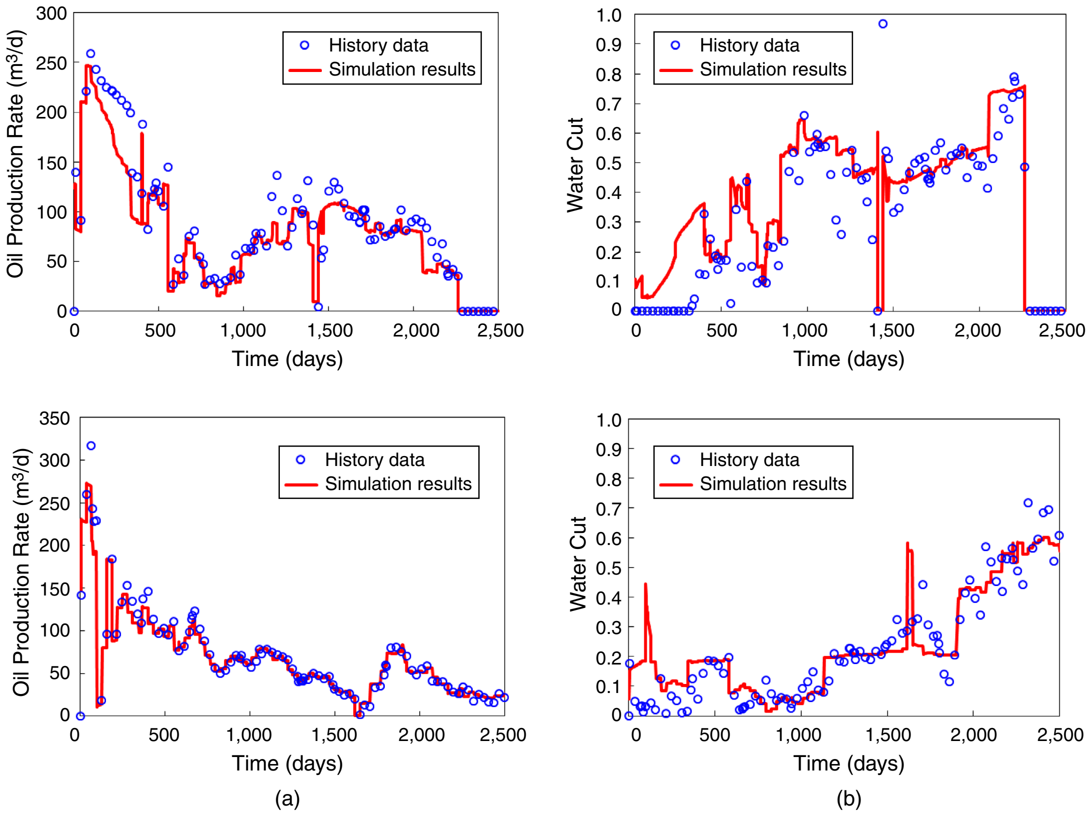

Fig. 27—Comparison of (a) oil production rate and (b) water cut for two representative wells between history data and simulation results after 2,500 days of production. The results in the first row is for one well, and those in the second row is for another well.

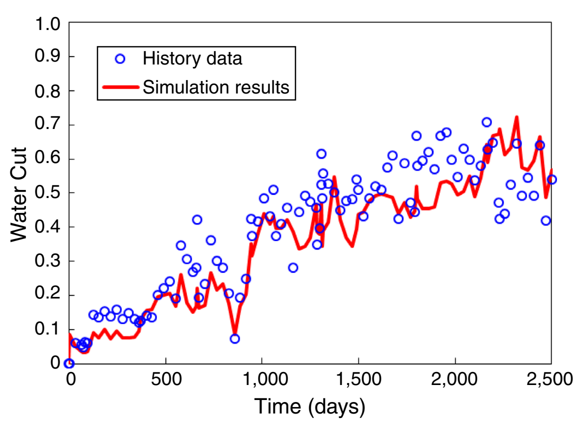

Fig. 28—Comparison of water cut for the whole reservoir between history data and simulation results after 2,500 days of production.

Conclusions

In this study, we presented an efficient hybrid model for 3D complex fractured vuggy reservoir simulation. In the hybrid model, a modified EDFM is proposed by using two sets of independent grids to discretize the matrix and fracture systems. Furthermore, on the basis of the assumption of instantaneous gravity differentiation, a simplified vug model is developed to model the coupled porous and free flow in the vuggy area. The validations are carried out which verify the two models. Then on the basis of the proposed hybrid model, a series of case studies are conducted, including three typical fracture-vug unit models and a real Tahe Oilfield Model. The following conclusions can be drawn from this work:

1. Compared with conventional EDFM, the computational cost of modified EDFM is higher because more fracture grids are generated in the modified EDFM. However, the gridding process of modified EDFM is more flexible, which avoids the 3D complex structure intersection problems in conventional EDFM. Moreover, the implementation of modified EDFM is easier.
2. The vug model can accurately describe the coupled porous and free flow in vuggy area, and, meanwhile, significantly decrease the computational complexity.
3. The simulation results of the three typical fracture-vug units show that fracture and vug have great influence on the flow character and production performance due to the high conductivity of fracture and the storage effect of vug.
4. The simulation of Tahe Oilfield reservoir model shows the good compatibility of the modified EDFM with corner-point grid, and the applicability of the hybrid model in fractured vuggy reservoirs with 3D complex fracture and vug geometries.

Nomenclature

A = interface area between elements, m^2
d = vertical distances from gridblock center to the interface, m
D = depth, m
$\boldsymbol{f}$ = unit vector from fracture interface to fracture center
g = gravitational acceleration, N·kg^{-1}
k = absolute permeability, m^2
k_{r} = relative permeability
$\tilde{k}_{r\beta}$ = relative permeability for vug flow
$\boldsymbol{n}$ = unit normal vector of fracture plane
p = pressure, Pa
p_c = capillary pressure, Pa
q = source/sink terms, kg·m^{-3}·s^{-1}
S = saturation
T = transmissibility between elements, m^3
V = element volume, m^3
V_v = volume of vug gridblock, m^3
Δt = timestep, seconds
η_n = all the neighbors of gridblock n
λ = fluid mobility, mPa^{-1}·s^{-1}
μ = viscosity, mPa·s
ρ = fluid density, kg·m^{-3}
ϕ = porosity
ψ = flow potential, Pa

Acknowledgments

The authors would like to thank the support of the Major science and technology projects of China National Petroleum Corporation (ZD2019-183-008), Fundamental Research Funds for the Central Universities (Nos. 18CX05029A, 19CX05002A, and 18CX07012A), National Science and Technology Major Project (2017ZX05009001), National Nature Science Foundation of China (Grant Nos. 51404292, 51676208, and 51936001).

References

Aziz, K. and Settari, A. 1979. *Petroleum Reservoir Simulation*. London, England, UK: Applied Science Publishers.

Beavers, G. S. and Joseph, D. D. 1967. Boundary Conditions at a Naturally Permeable Wall. *J Fluid Mech* **30** (1): 197–207. https://doi.org/10.1017/S0022112067001375.

Camacho-Velazquez, R., Vasquez-Cruz, M., Castrejon-Aivar, R. et al. 2002. Pressure Transient and Decline Curve Behaviors in Naturally Fractured Vuggy Carbonate Reservoirs. Paper presented at the SPE Annual Technical Conference and Exhibition, San Antonio, Texas, USA, 29 September–2 October. SPE-77689-MS. https://doi.org/10.2118/77689-MS.

Chen, Z. X. 1989. Transient Flow of Slightly Compressible Fluids through Double-Porosity, Double-Permeability Systems—A State-of-the-Art Review. *Trans Porous Media* **4** (2): 147–184. https://doi.org/10.1007/BF00134995.

Fumagalli, A., Pasquale, L., Zonca, S. et al. 2016. An Upscaling Procedure for Fractured Reservoirs with Embedded Grids. *Water Resour Res* **52** (8): 6506–6525. https://doi.org/10.1002/2015WR017729.

Guo, J. C., Nie, R. S., and Jia, Y. L. 2012. Dual Permeability Flow Behavior for Modeling Horizontal Well Production in Fractured-Vuggy Carbonate Reservoirs. *J Hydrol* **464:** 281–293. https://doi.org/10.1016/j.jhydrol.2012.07.021.

Huang, Z., Gao, B., Zhang, X. et al. 2016. On the Coupling of Two-Phase Free Flow and Porous Flow. Paper presented at the ECMOR XV-15th European Conference on the Mathematics of Oil Recovery, Amsterdam, The Netherlands, 29 August. https://doi.org/10.3997/2214-4609.201601774.

Huang, Z., Yan, X., and Yao, J. 2014. A Two-Phase Flow Simulation of Discrete-Fractured Media Using Mimetic Finite Difference Method. *Commun Comput Phy* **16** (3): 799–816. https://doi.org/10.4208/cicp.050413.170314a.

Huang, Z., Yao, J., Li, Y. et al. 2011. Numerical Calculation of Equivalent Permeability Tensor for Fractured Vuggy Porous Media Based on Homogenization Theory. *Commun Comput Phys* **9** (1): 180–204. https://doi.org/10.4208/cicp.150709.130410a.

Kang, Z., Wu, Y. S., Li, J. et al. 2006. Modeling Multiphase Flow in Naturally Fractured Vuggy Petroleum Reservoirs. Paper presented at the SPE Annual Technical Conference and Exhibition, San Antonio, Texas, USA, 24–27 September. SPE-102356-MS. https://doi.org/10.2118/102356-MS.

Karimi-Fard, M., Durlofsky, L. J., and Aziz, K. 2004. An Efficient Discrete-Fracture Model Applicable for General-Purpose Reservoir Simulators. *SPE J*. **9** (2): 227–236. SPE-88812-PA. https://doi.org/10.2118/88812-PA.
Lee, S. H., Jensen, C. L., and Lough, M. F. 1999. An Efficient Finite Difference Model for Flow in a Reservoir with Multiple Length-Scale Fractures. *SPE J*. **5** (3): 268–275. SPE-56752-MS. https://doi.org/10.2118/56752-MS.
Lee, S. H., Lough, M. F., and Jensen, C. L. 2001. Hierarchical Modeling of Flow in Naturally Fractured Formations with Multiple Length Scales. *Water Resour Res* **37** (3): 443–455. https://doi.org/10.1029/2000WR900340.
Li, L. and Lee, S. H. 2008. Efficient Field-Scale Simulation of Black Oil in a Naturally Fractured Reservoir through Discrete Fracture Networks and Homogenized Media. *SPE Res Eval & Eng* **11** (4): 750–758. SPE-103901-PA. https://doi.org/10.2118/103901-PA.
Lie, K. A. 2014. *An Introduction to Reservoir Simulation Using MATLAB: User Guide for the Matlab Reservoir Simulation Toolbox (MRST)*. Oslo, Norway: SINTEF ICT. https://www.sintef.no/contentassets/8af8db2e42614f7fb94fb0c68f5bc256/mrst-book-2016.pdf.
Liu, J., Bodvarsson, G. S., and Wu, Y. S. 2003. Analysis of Flow Behavior in Fractured Lithophysal Reservoirs. *J Contam Hydrol* **62** (1): 189–211. https://doi.org/10.1016/S0169-7722(02)00169-9.
Loucks, R. G. 1999. Paleocave Carbonate Reservoirs: Origins, Burial-Depth Modifications, Spatial Complexity, and Reservoir Implications. *AAPG Bull* **83** (11): 1795–1834. https://doi.org/10.1306/E4FD426F-1732-11D7-8645000102C1865D.
Lyu, X., Liu, Z., Hou, J. et al. 2017. Mechanism and Influencing Factors of EOR by N_2 Injection in Fractured-Vuggy Carbonate Reservoirs. *J Nat Gas Sci Eng* **40:** 226–235. https://doi.org/10.1016/j.jngse.2017.02.022.
Moinfar, A., Varavei, A., Sepehrnoori, K. et al. 2014. Development of an Efficient Embedded Discrete Fracture Model for 3D Compositional Reservoir Simulation in Fractured Reservoirs. *SPE J*. **19** (2): 289–303. SPE-154246-PA. https://doi.org/10.2118/154246-PA.
Panfili, P. and Cominelli, A. 2014. Simulation of Miscible Gas Injection in a Fractured Carbonate Reservoir Using an Embedded Discrete Fracture Model. Paper presented at the Abu Dhabi International Petroleum Exhibition and Conference, Abu Dhabi, UAE, 10–13 November. SPE-171830-MS. https://doi.org/10.2118/171830-MS.
Popov, P., Efendiev, Y., and Qin, G. 2009. Multiscale Modeling and Simulations of Flows in Naturally Fractured Karst Reservoirs. *Commun Comput Phys* **6** (1): 162–184. https://doi.org/10.4208/cicp.2009.v6.p162.
Quandalle, P. and Sabathier, J. C. 1989. Typical Features of a Multipurpose Reservoir Simulator. *SPE J*. **4** (4): 475–480. SPE-16007-PA. https://doi.org/10.2118/16007-PA.
Saffman, P. G. 1971. On the Boundary Condition at the Surface of a Porous Medium. *Stud Appl Math* **50** (2): 93–101. https://doi.org/10.1002/sapm197150293.
Smosna, R., Bruner, K. R., and Riley, R. A. 2005. Paleokarst and Reservoir Porosity in the Ordovician Beekmantown Dolomite of the Central Appalachian Basin. *Carbonates Evaporites* **20** (1): 50–63. https://doi.org/10.1007/BF03175448.
Warren, J. E. and Root, P. J. 1963. The Behavior of Naturally Fractured Reservoirs. *SPE J*. **3** (3): 245–255. SPE-426-PA. https://doi.org/10.2118/426-PA.
Wu, Y. S., Di, Y., Kang, Z. et al. 2011. A Multiple-Continuum Model for Simulating Single-Phase and Multiphase Flow in Naturally Fractured Vuggy Reservoirs. *J Pet Sci Eng* **78** (1): 13–22. https://doi.org/10.1016/j.petrol.2011.05.004.
Xie, H., Li, A., Huang, Z. et al. 2017. Coupling of Two-Phase Flow in Fractured-Vuggy Reservoir with Filling Medium. *Open Phy* **15** (1): 12–17. https://doi.org/10.1515/phys-2017-0002.
Xu, Y., Cavalcante Filho, J., Yu, W. et al. 2017. Discrete-Fracture Modeling of Complex Hydraulic-Fracture Geometries in Reservoir Simulators. *SPE Res Eval & Eng* **20** (2): 403–422. SPE-183647-PA. https://doi.org/10.2118/183647-PA.
Xu, Y., Fernandes, B. R. B., Marcondes, F. et al. 2019. Embedded Discrete Fracture Modeling for Compositional Reservoir Simulation Using Corner-Point Grids. *J Pet Sci Eng* **177** (2019): 41–52. https://doi.org/10.1016/j.petrol.2019.02.024.
Xu, Y. and Sepehrnoori, K. 2019. Development of an Embedded Discrete Fracture Model for Field-Scale Reservoir Simulation with Complex Corner-Point Grids. *SPE J*. **24** (4): 1552–1575. SPE-195572-PA. https://doi.org/10.2118/195572-PA.
Yan, X., Huang, Z., Yao, J. et al. 2018. An Efficient Numerical Hybrid Model for Multiphase Flow in Deformable Fractured-Shale Reservoirs. *SPE J*. **23** (4): 1412–1437. SPE-191122-PA. https://doi.org/10.2118/191122-PA.
Yan, X., Huang, Z., Yao, J. et al. 2019. Numerical Simulation of Hydro-Mechanical Coupling in Fractured Vuggy Porous Media Using the Equivalent Continuum Model and Embedded Discrete Fracture Model. *Adv Water Resour* **126:** 137–154. https://doi.org/10.1016/j.advwatres.2019.02.013.
Yao, J., Huang, Z., Li, Y. et al. 2010. Discrete Fracture-Vug Network Model for Modeling Fluid Flow in Fractured Vuggy Porous Media. Paper presented at the International Oil and Gas Conference and Exhibition, Beijing, China, 8–10 June. SPE-130287-MS. https://doi.org/10.2118/130287-MS.
Zhang, Q., Huang, Z., Yao, J. et al. 2017. Multiscale Mimetic Method for Two-Phase Flow in Fractured Media Using Embedded Discrete Fracture Model. *Adv Water Resour* **107:** 180–190. https://doi.org/10.1016/j.advwatres.2017.06.020.

Lijun Liu is a PhD-degree candidate in petroleum engineering at China University of Petroleum (East China). His research focuses on coupled multiphase/multicomponent flow and geomechanics in fractured vuggy reservoirs. Liu holds a bachelor's degree from the Petroleum Engineering Department at China University of Petroleum (East China).

Zhaoqin Huang is an associate professor in the Department of Reservoir Engineering at China University of Petroleum (East China). His research focuses on the multiscale and multiphysics modeling of transport phenomena in porous media. Huang holds a PhD degree in petroleum engineering and bachelor's and master's degrees in civil engineering from China University of Petroleum (East China).

Jun Yao is a professor and director of the Center of Multiphase Flow in Porous Media in the Department of Reservoir Engineering at China University of Petroleum (East China). His research interests include multiscale and multiphysics modeling of multiphase flow in porous media, numerical reservoir simulation, numerical well testing, and smart oilfield theory. Yao holds bachelor's, master's, and PhD degrees in petroleum engineering from China University of Petroleum (East China).

Yuan Di is an associate professor in the Department of Energy and Resources Engineering at Peking University. His research interests include numerical simulation of multiphase flow in porous media, wave propagation in porous media, and analysis of borehole stability. Di holds a bachelor's degree in civil engineering from Xi'an Jiaotong University, a master's degree in civil engineering from Xi'an University of Architecture and Technology, and a PhD degree in civil engineering from Tongji University.

Yu-Shu Wu is a professor, Foundation CMG Reservoir Modeling Chair, and director of the Energy Modeling Group Research Center in the Petroleum Engineering Department at the Colorado School of Mines. Previously, he was a staff scientist with the Earth Sciences Division of the Lawrence Berkeley National Laboratory for 14 years from 1995 to 2008. Wu's research interests include multiphase fluid and heat flow, geomechanics, unconventional-oil/gas-reservoir dynamics, CO_2 geosequestration and enhanced oil recovery, geothermal engineering, and numerical reservoir simulation. He is a fellow of the Geological Society of America and a Distinguished Member of SPE.